THE JOURNAL OF PHYSICAL CHEMISTRY C

Article

pubs.acs.org/JPCC

Surface Reconstruction and Reactivity of Platinum–Iron Oxide Nanoparticles

Paul N. Duchesne,[†] Guangxu Chen,[‡] Xiaojing Zhao,[‡] Nanfeng Zheng,[‡] and Peng Zhang*[,†]

[†]Department of Chemistry, Dalhousie University, 6274 Coburg Road, PO Box 15000, Halifax, Nova Scotia B3H 4R2, Canada

[‡]State Key Laboratory for Physical Chemistry of Solid Surfaces, and Collaborative Innovation Center of Chemistry for Energy Materials, College of Chemistry and Chemical Engineering, Xiamen University, Xiamen 361005, China

ABSTRACT: The electrochemical stability of platinum–iron oxide nanoparticles has been studied using X-ray absorption spectroscopy. Samples were monitored for changes in their surface structure and elemental composition after electrochemical cycling in acidic media, which were then correlated with their electronic properties and a thorough analysis of their electrocatalytic activities. In addition to the observation of significant surface restructuring, greater Fe content following electrochemical treatment was found to be associated with higher half-wave potentials and specific current densities (up to 0.965 ± 0.001 V_{RHE} and 1.32 ± 0.03 × 10^{-5} mA cm^{-2}, respectively). This work highlights the potential to improve the electrocatalytic activity of platinum–iron oxide nanoparticles by controlling the Fe content and platinum–iron bonding, and demonstrates the critical importance of characterizing these nanocatalysts both before and after use.

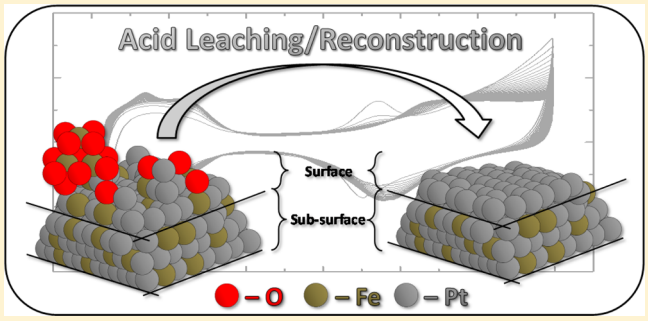

1. INTRODUCTION

In the field of renewable energy research, fuel cells are a subject of considerable interest. Like batteries, fuel cells allow energy to be stored for future use, which is an essential step in the development of alternative energy infrastructures.[1] Although a number of different fuel cell chemistries exist, polymer electrolyte membrane fuel cells (PEMFCs) offer several distinct advantages, including minimal emissions (pure water), low operating temperatures, and high energy densities, making them particularly appealing for implementation in motor vehicles.[2,3] In PEMFCs, the electrical energy is generated by the formation of water from gaseous hydrogen and oxygen. This process comprises the hydrogen oxidation and oxygen reduction reactions (HOR and ORR), which, respectively, occur at the fuel cell anode and cathode. While the cathodic HOR is well-catalyzed using standard Pt catalyst materials and loading, efficiently catalyzing the anodic ORR has proven more challenging;[4] as a result, the kinetics of the overall reaction are limited by the ORR, making the development of superior anode catalysts the focus of considerable research efforts.[5−7] One major obstacle to the development of ORR catalysts is the cost of such systems, due largely to the expensive, typically Pt-based electrode catalysts required for efficient conversion of fuel to electricity. In principle, this could be offset by incorporating non-noble metals and/or increasing the electrochemically active surface area (ECSA) of the catalyst material.

One method of accomplishing this cost reduction is to form alloyed or composite Pt-based nanoparticles capable of preserving (or even enhancing) the catalytic activity of Pt while simultaneously reducing material costs.[3,8−10] Unfortunately, the non-noble components of these nanoparticles are also inherently less stable under standard fuel cell operating conditions (strong electrical potentials, corrosive electrolytes, etc.), and may be prone to leaching.[11,12] As a result, it is entirely possible that the structure of the active catalyst differs significantly from its as-synthesized form. The effect of leaching on surface structure has been explored using various Pt-3d metal alloys, revealing that such processes lead to the formation of a Pt-enriched "skin" due to the lesser stability on the non-noble metal component.[5,13,14] Interestingly, some of the same studies also revealed an enrichment of the 3d metal in the first sublayer of metal atoms, which is implicated in the enhanced activity of such surfaces.[5] Furthermore, activity studies performed on monocrystalline (111), (110), and (100) surfaces revealed their differential activities with respect to the ORR.[5] Thus, knowledge of the surface structure of a material becomes a vital factor when attempting to synthesize new electrode catalysts.

Unfortunately, surface characterization of catalysts can prove to be a challenging proposition. Depending on the size and geometry of the surface being studied, the proportion of surface atoms in a sample may range from a majority (in small nanoclusters) to nearly negligible (in bulk materials). As a result, studying these surfaces requires the use of specialized techniques. Electrochemical methods have previously been used to study the surfaces of metal nanoparticles,[15,16] and can

Received: September 12, 2014
Revised: November 14, 2014
Published: November 15, 2014

   dx.doi.org/10.1021/jp509264a | J. Phys. Chem. C 2014, 118, 28861−28867

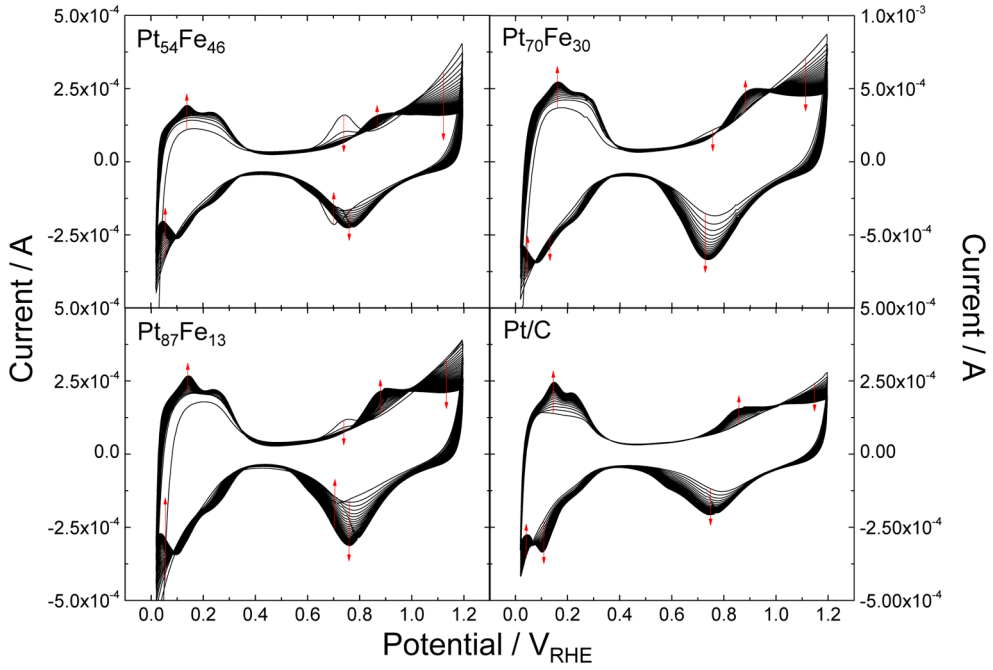

Figure 1. Evolution of cyclic voltammograms from $PtFeO_x$ and Pt/C reference samples over 50 cycles. Red arrows indicate the direction of change for each region of interest.

prove particularly useful for those which function as catalysts.[13,17] Despite this utility, more accurate information regarding the local structure of surfaces is beyond the scope of such experiments; however, such information can be obtained through the use of X-ray absorption spectroscopy (XAS). XAS allows for element-specific characterization and is well-suited for the study of nanoparticle samples, as has been demonstrated in previous studies.[18−20]

Herein we compare a series of carbon-supported platinum−iron oxide ($Pt-FeO_x$) nanoparticles before and after electrochemical cycling in acidic electrolyte. In addition to observing any gross changes to the particles themselves using transmission electron microscopy (TEM), changes in their local structure and electronic properties are elucidated through the analysis of extended X-ray absorption fine structure (EXAFS) and X-ray absorption near-edge structure (XANES) data. A more thorough investigation of the electrocatalytic activities of these samples is also undertaken. All of these results provide deeper insights into the correlation between the structure and activity of Pt catalysts following electrochemical cycling in acidic media.

2. EXPERIMENTAL METHODS

2.1. Sample Preparation. $Pt-FeO_x$ nanoparticles were synthesized using a facile, "clean" method that has been published previously.[21] Briefly, these nanoparticles were formed at elevated temperatures in oleylamine (OAm) solution under a reducing atmosphere of carbon monoxide. Control of the Pt:Fe ratio in the reaction mixture was used to generate nanoparticles with differing elemental compositions. Surface-capping OAm ligands were removed via ligand exchange with excess *n*-butylamine in the presence of suspended Vulcan XC-72 carbon powder, inducing immobilization of the nanoparticles onto the carbon support (30% mass loading). Catalyst loading was measured using inductively coupled plasma optical emission spectroscopy. A commercial Pt catalyst (HiSPEC 3000, 20% mass loading, denoted "Pt/C") was also used as a reference during characterization of the $Pt-FeO_x$ samples.

Following electrochemical characterization, samples of the post-treatment $Pt-FeO_x$ and Pt/C materials were obtained for further XAS analysis. First, the rotating disk electrode (RDE) was removed from the electrolyte solution and carefully dried by wicking away any residual liquid with the edge of a Kimwipe tissue. After allowing the sample several minutes to dry, a strip of cellophane tape was applied to the surface of the glassy carbon RDE; removing the tape also removed a thin, but appreciable, layer of sample. This was repeated several times to ensure collection of sufficient material before the exposed sample was sealed-in with a second strip of tape.

2.2. Voltammetry Characterization. A Pine Instrument Company RDE) system was used to perform electrochemical measurements. Full experimental details have been presented previously.[21] In brief, a three-electrode cell was assembled consisting of a glassy carbon RDE working electrode, Pt wire counter electrode, and Koslow mercury/mercurous sulfate reference electrode in 0.1 M perchloric acid electrolyte. Glassware was decontaminated by boiling in deionized water prior to use. Measurements were then conducted according to standard procedures.[11]

To investigate the effects of electrochemical treatment on $Pt-FeO_x$ nanoparticles, samples in $Ar_{(g)}$-saturated electrolyte were exposed to applied potentials between 0.02 and 1.2 V versus a reversible hydrogen electrode (V_{RHE}). The treatment continued for 50 cycles at a sweep rate of 50 mV_{RHE} s^{-1}. The activity of each sample with regards to the oxygen reduction reaction (ORR) was measured by saturating the electrolyte solution with $O_{2(g)}$ and then sweeping the applied potential over the same potential range used for the initial electrochemical treatment. A rotation rate of 1600 rpm was used for all experiments. Area-specific current densities were obtained by correcting these experimental data to account for key factors, including non-Faradaic contributions, mass transport at the

dx.doi.org/10.1021/jp509264a | J. Phys. Chem. C 2014, 118, 28861−28867

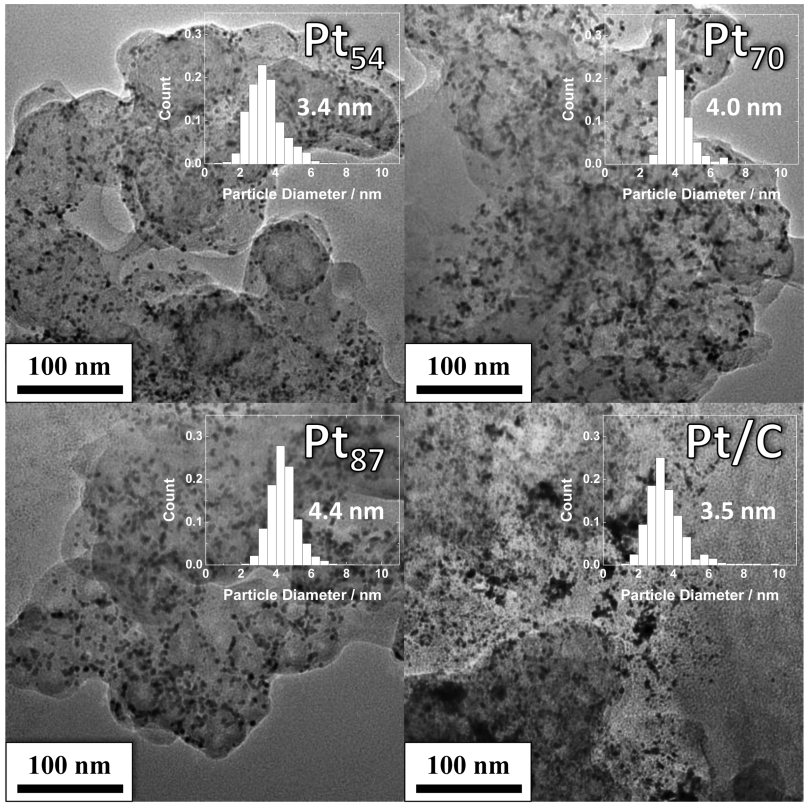

Figure 2. TEM micrographs of post-treatment $PtFeO_x$ and reference Pt/C catalyst samples. Inset histograms depict measured nanoparticle diameters as measured from a series of images ($444 < N < 599$).

electrode surface, and electrochemically active surface area (ECSA) for each sample.[22]

2.3. X-ray Absorption Spectroscopy. XAS data acquisition was performed using BM-20 of the Advanced Photon Source, located at Argonne National Laboratory, Argonne, IL. A double-crystal Si(111) mirror monochromator was used for wavelength selection and detuned to 80% in order to reject higher harmonics. Standard gas-ionization chamber detectors were used for reference foil data, whereas the limited quantity of both the Pt−FeO_x and Pt/C samples necessitated the use of a more sensitive a 32-element Ge fluorescence detector. A cryostatic sample holder was used to maintain a stable temperature of 50 ± 1 K (pretreatment samples) or 90 ± 1 (post-treatment samples) in order to further enhance the intensity of the EXAFS data signal via suppression of thermal vibrations, thereby obtaining better signal-to-noise ratios. Processing and fitting of XAS data were performed using the IFEFFIT software suite.[23]

2.4. Transmission Electron Microscopy. Due to the fact that they had been preserved between strips of cellophane tape, preparing the post-treatment nanoparticle samples for TEM analysis required some work. After carefully separating the strips of tape encompassing the post-treatment sample material, both strips were inserted into a small (1.5 mL) sample vial filled with *n*-hexane and sonicated until their adhesive dissolved, releasing the sample from the cellophane backing. The undissolved cellophane backing was then carefully removed, and the remaining suspension was centrifuged at 15 000 rpm for 5 min to separate the sample material from the supernatant, which was then decanted. Each sample was then washed once with 1 mL of laboratory grade ethanol (i.e., sonicated, then centrifuged again under the same conditions). Finally, each sample was dispersed in 200 uL of ethanol via sonication and drop-cast onto Formvar-coated copper TEM grids. Sample imaging was performed using a Tecnai F-30 transmission electron microscope operated at 300 kV in bright-field imaging mode. Size distributions of the nanoparticles were measured using MacBiophotonics ImageJ software and several representative images from each sample.[24]

3. RESULTS AND DISCUSSION

3.1. Cyclic Voltammetry Treatment and Characterization. Cyclic voltammograms (CVs) of both the Pt−FeO_x samples and Pt/C reference catalyst are presented in Figure 1. After 50 cycles, marked changes were observed in the CVs over several regions of interest. Most of these regions are characteristic of Pt, but peaks attributable to the oxidation (ca. 0.74 V_{RHE}, forward sweep) and reduction (ca. 0.7 V_{RHE}, reverse sweep) of the Fe^{2+}/Fe^{3+} redox couple were apparent in the Pt−FeO_x CVs.[25] In general, it was observed that peaks indicative of H-adsorption/desorption (0.5−3.5 V_{RHE}) and Pt-surface reduction peaks increased in intensity, $H_{2(g)}$ evolution (0−0.5 V_{RHE}) decreased in intensity, and Pt-surface oxidation shifted to more negative potentials. These changes are consistent with restructuring of the Pt surface as a result of potential cycling, and indicate the emergence of distinct Pt(111) and Pt(110) crystallographic facets from a more irregular initial structure.[15] Peaks associated with the Fe^{2+}/Fe^{3+} redox couple were observed to disappear after only a few scans, suggesting that these species were present at the Pt surface and dissolved readily into the acidic electrolyte solution. As expected, the most intense Fe^{2+}/Fe^{3+} feature was observed for $Pt_{54}Fe_{46}$, which has the greatest Fe content; however, the $Pt_{70}Fe_{30}$ sample did not exhibit intermediate peak intensity

dx.doi.org/10.1021/jp509264a | J. Phys. Chem. C 2014, 118, 28861−28867

between the former sample and $Pt_{87}Fe_{13}$, as might have been expected given its relative composition. This indicates that less Fe-oxide was present at the surfaces of the $Pt_{70}Fe_{30}$ nanoparticles and, by extension, that Fe was more successfully incorporated into the metallic Pt core. In contrast with that located at the nanoparticle surface, Fe located in the core should be both physically shielded from the acidic electrolyte and electronically stabilized by its Pt neighbors.

3.2. Transmission Electron Microscopy. TEM images (see Figure 2) were acquired for each nanoparticle sample in order to ensure no drastic changes in morphology had occurred as a result of the electrochemical treatment. In fact, very little change was observed, with particle sizes of 3.5 ± 1.2 nm, 3.4 ± 1.0 nm, 4.0 ± 0.8 nm, and 4.5 ± 0.8 nm being observed for Pt/C, $Pt_{54}Fe_{46}$, $Pt_{70}Fe_{30}$, and $Pt_{87}Fe_{13}$, respectively. These values match closely with those determined for the samples prior to electrochemical treatment (2.8 ± 0.7 nm, 3.5 ± 0.5 nm, 4.0 ± 0.5 nm, and 4.4 ± 0.6 nm), suggesting that significant particle aggregation did not occur during electrochemical cycling. Close analysis of the TEM images reveals that some fusion of adjacent particles to form oblong, rodlike structures did occur for a small number of particles; however, such behavior has been reported previously and does not appear to degrade catalyst performance as does the formation of large, spherical aggregates.[26] Overall, only minor structural changes can be confirmed by the results of TEM analysis.

3.3. X-ray Absorption Spectroscopy Characterization. XAS measurements were performed at the Pt L_3 absorption edge in order to study Pt−FeO_x and Pt/C catalyst samples both before and after electrochemical cycling. XANES spectra from these measurements are presented in Figure 3. Although the

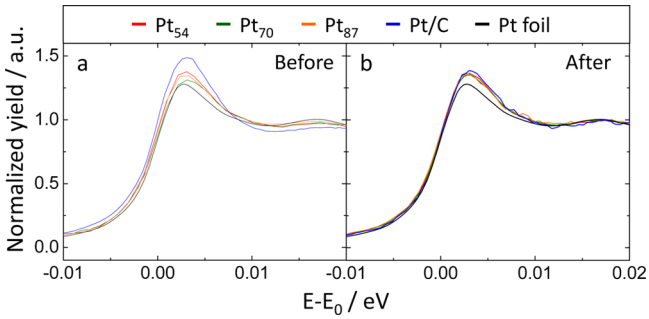

Figure 3. Comparisons of Pt L_3-edge XANES spectra acquired (a) before (at 50 K) and (b) after (at 90 K) electrochemical treatment in 0.1 M $HClO_{4(aq)}$ electrolyte.

Pt−FeO_x samples appear to have behaved differently with regards to electrochemical treatment, the changes observed can provide useful insight into their structure. Both $Pt_{54}Fe_{46}$ and $Pt_{87}Fe_{13}$ samples exhibited little change in white line (the intense peak following the absorption edge) shape or intensity as a result of treatment, indicating that changes to the average Pt environment in these samples were minimal. In contrast, the white line intensity of $Pt_{70}Fe_{30}$ increased slightly post-treatment, while that of Pt/C decreased. From a basic understanding of XANES principles, these changes can be interpreted as arising from changes in the Pt *d*-electron density (decreased electron density results in increased white line intensity).[27] This decreased electron density of Pt in $Pt_{70}Fe_{30}$ after electrochemical treatment may be related to the loss of charge transfer from Fe to Pt atoms in the nanoparticles. The fact that the Pt electron density is reduced as a result of treatment could indicate that a significant amount of metallic Fe near the surface was removed from the nanoparticles alongside the surface Fe-oxides. This is also consistent with the conclusion that the $Pt_{70}Fe_{30}$ sample contains a relatively greater amount of metallic Fe than the other Pt−FeO_x samples. The increase in *d*-electron density experienced by Pt/C should not be due to leaching of its components (primarily Pt and O) as do the Pt−FeO_x samples, but could be explained by a reduction of oxidized surface Pt. In order to better understand the root causes for these changes, it is helpful to closely study the local structure of each sample.

Fourier-transformed EXAFS spectra for Pt−FeO_x samples and Pt/C are presented in Figure 4. Despite being obtained at a

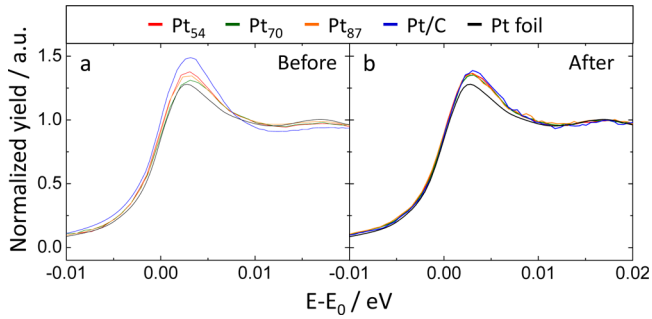

Figure 4. Comparisons of Fourier-transformed Pt L_3-edge EXAFS spectra for Pt−FeO_x and Pt/C samples acquired (a) before and (b) after electrochemical treatment.

higher temperature (90 ± 1 K, versus 50 ± 1 K for the untreated data), the postcycling spectra exhibited qualitatively more intense peaks corresponding to Pt-M scattering paths. As the unusually low intensity observed for the Pt-M paths prior to cycling has been attributed to destructive interference between Pt-Pt and Pt-Fe scattering paths, this increased intensity could be understood as a decrease in one of these two contributions to the overall peak intensity. Furthermore, the overall qualitative similarity of the EXAFS spectra, especially at higher *R*-values, indicates that the samples have become more structurally similar. Differences introduced during sample synthesis appear to have been thus homogenized by the electrochemical cycling process. Additionally, the intensity reduction of the Pt−O peak of Pt/C (ca. 1.7 Å) indicates that less Pt-oxide is present post-treatment, further supporting the reduction of surface Pt based on XANES analysis (see above). In order to fully characterize the structural changes in these samples, fitting of experimental EXAFS spectra was performed.

Experimental and fitted Fourier-transformed EXAFS spectra are presented in Figure 5. Corresponding structural parameters obtained from the fitting of pre- and post-treatment Pt−FeO_x and Pt/C samples are presented in Table 1. Immediately apparent from these data is the significant decrease in the degree of Pt−Fe bonding after electrochemical cycling. As indicated by their respective Pt−Fe coordination numbers (CNs), both $Pt_{70}Fe_{30}$ and $Pt_{87}Fe_{13}$ retained a measurable degree of Pt−Fe interaction. Given the structural information available from cyclic voltammetry and XANES analyses, this is likely due to the relatively large amount of metallic Fe located at or beneath the Pt surface of its constituent nanoparticles. Further support for this conclusion is afforded by the observed Pt−Fe bond lengths. For the pretreatment samples, it was observed that the mean Pt−Fe bond length was correlated with greater Fe content. On the basis of the Fe K-edge XANES results from

dx.doi.org/10.1021/jp509264a | J. Phys. Chem. C 2014, 118, 28861−28867

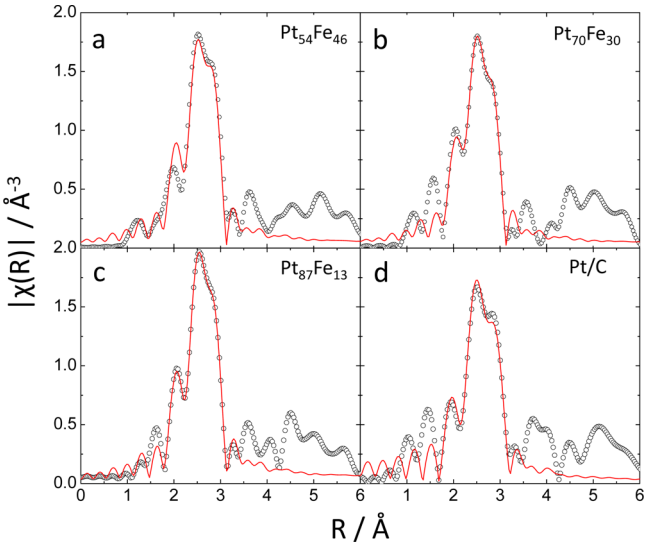

Figure 5. Fourier-transformed experimental (hollow circles) and fitted (red lines) EXAFS spectra for electrochemically treated (a) $Pt_{54}Fe_{46}$, (b) $Pt_{70}Fe_{30}$, (c) $Pt_{87}Fe_{13}$, and (d) Pt/C samples.

the as-synthesized Pt−FeO_x,[21] samples with greater Fe content also possessed relatively more Fe-oxide than metallic Fe. Thus, it can be inferred that a predominance of metallic Pt−Fe interactions yields shorter average bond lengths (ca. 2.67 Å) than does that of oxide Pt−Fe interactions (ca. 2.72 Å). Therefore, the relatively short Pt−Fe bond length for postcycling $Pt_{70}Fe_{30}$ indicates that the remaining Fe is likely present in a metallic environment.

With regards to the observed Pt-Pt CNs, an increase was observed for all samples as a result of electrochemical cycling. This is easily explained by surface reconstruction, as is indicated by the evolution of characteristic H-adsorption/desorption peaks in the CVs for each sample. From the low Pt-Fe and Pt-Pt CNs obtained prior to treatment, it appears that both the Pt−FeO_x samples and Pt/C catalyst possessed irregular or defected surface morphologies in their as-synthesized forms, likely facilitated by the presence of a stabilizing surface Fe oxide layer. The harsh conditions introduced by electrochemical cycling have clearly proven sufficient to effect considerable transformation on initial structure, resulting in higher CNs reflective of a more uniform Pt lattice.

3.4. ORR Activity Testing. The ORR activities of the Pt−FeO_x and Pt/C samples were evaluated via linear sweep voltammetry, with the resultant normalized current densities and Tafel plots presented in Figure 6. By further correcting for mass-transfer limited diffusion using the Levich relation,[11] reliable measures of specific current density ($j_{specific}$) under kinetically controlled conditions (0.95 V_{RHE} applied potential) were obtained. Half-wave potentials ($E_{1/2}$, measured at one-half the maximum diffusion-limited current density) are generally indicative of the thermodynamic efficiency (or voltage efficiency) of an electrochemical reaction.[28] In the case of ORR activity, a more positive potential is indicative of a lower overpotential required to drive the reaction, and thus a higher efficiency. Tafel plots were also prepared and fitted using linear regression in order to obtain their characteristic Tafel slopes. Experimentally determined values of $E_{1/2}$, $j_{specific}$, and Tafel slope for each sample are presented in Table 2.

From these data, it is clear that $Pt_{70}Fe_{30}$ exhibits the largest $E_{1/2}$ of the four samples tested (0.965 ± 0.001 V_{RHE}), followed by $Pt_{87}Fe_{13}$ (0.939 ± 0.001 V_{RHE}), $Pt_{54}Fe_{46}$ (0.917 ± 0.001 V_{RHE}), and Pt/C (0.913 ± 0.001 V_{RHE}). In terms of $j_{specific}$, $Pt_{70}Fe_{30}$ also offered the highest kinetic current density (1.32 ± 0.03 × 10^{-1} mA·cm^{-2}). In keeping with previous findings, $Pt_{87}Fe_{13}$ also offers the next best $j_{specific}$ (9.9 ± 0.2 × 10^{-2} mA·cm^{-2}) but is not significantly better than $Pt_{54}Fe_{46}$ (also 9.8 ± 0.3 × 10^{-2} mA·cm^{-2}), and Pt/C again demonstrates the poorest performance (just 7.1 ± 0.2 × 10^{-2} mA·cm^{-2}). One possible explanation for the similar $j_{specific}$ values of $Pt_{87}Fe_{13}$ and $Pt_{54}Fe_{36}$, despite the larger $E_{1/2}$ of the former, is that both two-electron ($O_2 + 2H^+ + 2e^- \rightarrow H_2O_2$) and four-electron ($O_2 + 4H^+ + 4e^- \rightarrow 2H_2O$) pathways exist for the reduction of $O_{2(g)}$ at Pt surfaces.[29] While the latter typically predominates, the former is also viable. It is thus proposed that the relatively greater $j_{specific}$ of $Pt_{54}Fe_{46}$ could be due to the competing two-electron formation of H_2O_2, thereby explaining its similar performance to $Pt_{87}Fe_{13}$ despite the differences in their local structures (as indicated by EXAFS analysis).

Experimentally, the reduction of $O_{2(g)}$ on Pt corresponds to Tafel slopes of approximately −60 mV_{RHE}·dec^{-1} at higher potentials (greater than 0.8 V_{RHE}) and −120 mV_{RHE}·dec^{-1} for measurements obtained at and lower potentials (less than 0.8 V_{RHE}).[30] This is explained by a difference in the rate-determining step of the ORR on Pt/Pt−O and pure metallic Pt surfaces, respectively. A comparison of the samples studied revealed slopes well in line with those published previously for Pt and PtFe nanoparticle samples,[3] with one exception. $Pt_{70}Fe_{30}$ demonstrated a Tafel slope 13% greater in magnitude than those of the other samples (−78 ± 1 mV_{RHE}·dec^{-1} versus ca. −68 ± 1 mV_{RHE}·dec^{-1}). The fact that all of these slopes differ from the ideal value for a mixed Pt/Pt−O surface may indicate that they possess significant areas of metallic Pt, with such areas comprising a significantly larger proportion of the $Pt_{70}Fe_{30}$

Table 1. Structural Parameters Obtained from Fitting of Pt L_3-Edge EXAFS Spectra Prior to, and Following, Electrochemical Cycling

		before treatment				after treatment			
sample	path	CN	R (Å)	σ^2 (10^{-3} Å^2)	ΔE_0 (eV)	CN	R (Å)	σ^2 (10^{-3} Å^2)	ΔE_0 (eV)
$Pt_{87}Fe_{13}$	Pt-Fe	1.0 ± 0.3	2.67 ± 0.02	3 ± 1	1 ± 2	0.6 ± 0.2	2.67 ± 0.01	3 ± 1	5 ± 1
	Pt-Pt	8 ± 1	2.775 ± 0.005			10 ± 1	2.75 ± 0.01		
$Pt_{70}Fe_{30}$	Pt-Fe	1.7 ± 0.7	2.70 ± 0.03	6 ± 2	2 ± 2	0.7 ± 0.6	2.67 ± 0.05	4 ± 1	4 ± 2
	Pt-Pt	7 ± 2	2.72 ± 0.01			11 ± 3	2.75 ± 0.01		
$Pt_{54}Fe_{46}$	Pt-Fe	1 ± 1	2.72 ± 0.09	3 ± 3	3 ± 4	**	**	4 ± 1	4 ± 2
	Pt-Pt	7 ± 3	2.72 ± 0.03			11 ± 2	2.75 ± 0.01		
Pt/C	Pt-O	1.9 ± 0.3	2.04 ± 0.02	2 ± 2	10 ± 1	**	**	3 ± 1	6 ± 1
	Pt-Pt	6 ± 2	2.78 ± 0.01			10 ± 1	2.76 ± 0.01		

dx.doi.org/10.1021/jp509264a | J. Phys. Chem. C 2014, 118, 28861−28867

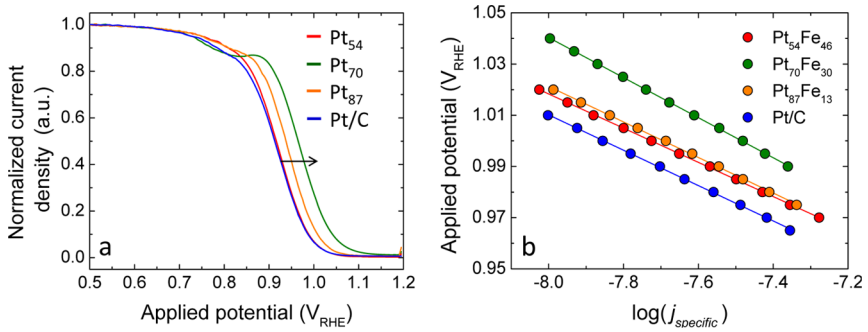

Figure 6. (a) Normalized specific current density and (b) Tafel plots of the Pt−FeO_x samples and Pt/C reference normalized by maximum diffusion-limited current (at 0.5 V).

Table 2. Figures of Merit for the ORR Activities of Pt−FeO_x and Pt/C Samples[a]

sample	half-wave potential (V_{RHE})	specific current density (10^{-2} mA·cm^{-2})	Tafel slope (mV$_{RHE}$·dec^{-1})
$Pt_{87}Fe_{13}$	0.939 ± 0.001	9.9 ± 0.2	−69 ± 1
$Pt_{70}Fe_{30}$	0.965 ± 0.001	13.2 ± 0.3	−78 ± 1
$Pt_{54}Fe_{46}$	0.917 ± 0.001	9.8 ± 0.3	−67 ± 1
Pt/C	0.913 ± 0.001	7.1 ± 0.2	−69 ± 1

[a]Uncertainties represent standard deviations (3σ) from the measured mean parameter values.

surface. This also agrees well with the results of EXAFS analysis, which rule out the existence of extensive surface oxide species.

4. CONCLUSIONS

In summation, XAS data analysis and electrochemical measurements have been used to study physical changes in Pt−FeO_x nanoparticles as a result of potential cycling in acidic media. It was found that, following the electrochemical treatment, the sample retaining an appreciable amount of Fe (the $Pt_{70}Fe_{30}$ sample) exhibited the best electrocatalytic activity. In addition to the impact of initial metallic Fe formation (and its diffusion into Pt nanoparticles) on electrocatalytic activity, subsequent reconstruction of the nanoparticle surface as a result of electrochemical treatment was also observed. Ultimately, these results demonstrate the critical importance of in situ or postoperative catalyst characterization and highlight the impact of diffusion-induced alloying in controlling the surface reactivity of Pt nanoparticles.

AUTHOR INFORMATION

Notes

The authors declare no competing financial interest.

ACKNOWLEDGMENTS

Financial support from NSERC Canada is graciously acknowledged. PNC/XSD facilities at the Advanced Photon Source (APS), and research at these facilities is supported by the U.S. Department of Energy - Basic Energy Sciences, a Major Resources Support grant from NSERC, the University of Washington, the Canadian Light Source, and the Advanced Photon Source. Use of the APS, an Office of Science User Facility operated for the U.S. Department of Energy (DOE), Office of Science, by Argonne National Laboratory, was supported by the U.S. DOE under Contract DE-AC02-06CH11357. Thanks are extended to beamline scientists Dr. Robert Gordon for his technical support and assistance in XAS data acquisition, and also to Timothy Crowtz from Prof. Jeff Dahn's group at Dalhousie University for his assistance in obtaining and interpreting electrochemical data. We also wish to acknowledge the Open Project (No. 201401) of The State Key Laboratory of Physical Chemistry of Solid Surfaces (Xiamen University) and the Visiting Scholar Program of iChEM (Xiamen University).

REFERENCES

(1) Ibrahim, H.; Ilinca, A.; Perron, J. Energy Storage Systems—Characteristics and Comparisons. *Renewable Sustainable Energy Rev.* **2008**, *12*, 1221−1250.

(2) Carrette, L.; Friedrich, K. A.; Stimming, U. Fuel Cells: Principles, Types, Fuels, and Applications. *ChemPhysChem* **2000**, *1*, 162−193.

(3) Mehta, V.; Cooper, J. S. Review and Analysis of PEM Fuel Cell Design and Manufacturing. *J. Power Sources* **2003**, *114*, 32−53.

(4) Oezaslan, M.; Hasché, F.; Strasser, P. Pt-Based Core−Shell Catalyst Architectures for Oxygen Fuel Cell Electrodes. *J. Phys. Chem. Lett.* **2013**, *4*, 3273−3291.

(5) Stamenkovic, V. R.; Fowler, B.; Mun, B. S.; Wang, G.; Ross, P. N.; Lucas, C. A.; Marković, N. M. Improved Oxygen Reduction Activity on Pt3Ni(111) via Increased Surface Site Availability. *Science* **2007**, *315*, 493−497.

(6) Yu, X.; Ye, S. Recent Advances in Activity and Durability Enhancement of Pt/C Catalytic Cathode in PEMFC. *J. Power Sources* **2007**, *172*, 133−144.

(7) Kim, J.; Lee, Y.; Sun, S. Structurally Ordered FePt Nanoparticles and Their Enhanced Catalysis for Oxygen Reduction Reaction. *J. Am. Chem. Soc.* **2010**, *132*, 4996−4997.

(8) Yang, L.; Shan, S.; Loukrakpam, R.; Petkov, V.; Ren, Y.; Wanjala, B. N.; Engelhard, M. H.; Luo, J.; Yin, J.; Chen, Y.; et al. Role of Support-Nanoalloy Interactions in the Atomic-Scale Structural and Chemical Ordering for Tuning Catalytic Sites. *J. Am. Chem. Soc.* **2012**, *134*, 15048−15060.

(9) Loukrakpam, R.; Luo, J.; He, T.; Chen, Y.; Xu, Z.; Njoki, P. N.; Wanjala, B. N.; Fang, B.; Mott, D.; Yin, J.; et al. Nanoengineered PtCo and PtNi Catalysts for Oxygen Reduction Reaction: An Assessment of the Structural and Electrocatalytic Properties. *J. Phys. Chem. C* **2011**, *115*, 1682−1694.

(10) Chen, G.; Zhao, Y.; Fu, G.; Duchesne, P. N.; Gu, L.; Zheng, Y.; Weng, X.; Chen, M.; Zhang, P.; Pao, C.-W.; et al. Interfacial Effects in Iron-Nickel Hydroxide-Platinum Nanoparticles Enhance Catalytic Oxidation. *Science* **2014**, *344*, 495−499.

(11) Gasteiger, H. A.; Kocha, S. S.; Sompalli, B.; Wagner, F. T. Activity Benchmarks and Requirements for Pt, Pt-Alloy, and Non-Pt Oxygen Reduction Catalysts for PEMFCs. *Appl. Catal., B* **2005**, *56*, 9−35.
(12) Pachón, L. D.; Rothenberg, G. Transition-Metal Nanoparticles: Synthesis, Stability and the Leaching Issue. *Appl. Organomet. Chem.* **2008**, *22*, 288−299.
(13) Toda, T.; Igarashi, H.; Watanabe, M. Enhancement of the Electrocatalytic O_2 Reduction on Pt−Fe Alloys. *J. Electroanal. Chem.* **1999**, *460*, 258−262.
(14) Bing, Y.; Liu, H.; Zhang, L.; Ghosh, D.; Zhang, J. Nanostructured Pt-Alloy Electrocatalysts for PEM Fuel Cell Oxygen Reduction Reaction. *Chem. Soc. Rev.* **2010**, *39*, 2184−2202.
(15) Gómez, R.; Orts, J. M.; Álvarez-Ruiz, B.; Feliu, J. M. Effect of Temperature on Hydrogen Adsorption on Pt (111), Pt (110), and Pt (100) Electrodes in 0.1 M $HClO_4$. *J. Phys. Chem. B* **2004**, *108*, 228−238.
(16) Chen, D.; Ye, J.; Xu, C.; Li, X.; Li, J.; Zhen, C.; Tian, N.; Zhou, Z.; Sun, S. Interaction of Citrate with Pt(100) Surface Investigated by Cyclic Voltammetry towards Understanding the Structure-Tuning Effect in Nanomaterials Synthesis. *Sci. China: Chem.* **2012**, *55*, 2353−2358.
(17) Tian, N.; Zhou, Z.-Y.; Sun, S.-G.; Ding, Y.; Wang, Z. L. Synthesis of Tetrahexahedral Platinum Nanocrystals with High-Index Facets and High Electro-Oxidation Activity. *Science* **2007**, *316*, 732−735.
(18) Bayindir, Z.; Duchesne, P. N.; Cook, S. C.; MacDonald, M. A.; Zhang, P. X-ray Spectroscopy Studies on the Surface Structural Characteristics and Electronic Properties of Platinum Nanoparticles. *J. Chem. Phys.* **2009**, *131* (244716), 1−6.
(19) Duchesne, P. N.; Zhang, P. Local Structure of Fluorescent Platinum Nanoclusters. *Nanoscale* **2012**, *4*, 4199−4205.
(20) Duchesne, P. N.; Zhang, P. Element-Specific Analysis of the Growth Mechanism, Local Structure, and Electronic Properties of Pt Clusters Formed on Ag Nanoparticle Surfaces. *J. Phys. Chem. C* **2014**, *118*, 21714−21721.
(21) Duchesne, P. N.; Chen, G.; Zheng, N.; Zhang, P. Local Structure, Electronic Behavior, and Electrocatalytic Reactivity of CO-Reduced Platinum−Iron Oxide Nanoparticles. *J. Phys. Chem. C* **2013**, *117*, 26324−26333.
(22) Liu, G. C.-K.; Sanderson, R. J.; Vernstrom, G.; Stevens, D. A.; Atanasoski, R. T.; Debe, M. K.; Dahn, J. R. RDE Measurements of ORR Activity of $Pt_{1-x}Ir_x$ ($0 < x < 0.3$) on High Surface Area NSTF-Coated Glassy Carbon Disks. *J. Electrochem. Soc.* **2010**, *157*, B207−B214.
(23) Ravel, B.; Newville, M. ATHENA, ARTEMIS, HEPHAESTUS: Data Analysis for X-ray Absorption Spectroscopy Using IFEFFIT. *J. Synchrotron Radiat.* **2005**, *12*, 537−541.
(24) Schneider, C. A.; Rasband, W. S.; Eliceiri, K. W. NIH Image to ImageJ: 25 Years of Image Analysis. *Nat. Methods* **2012**, *9*, 671−675.
(25) Atkins, P.; de Paula, J. Data Section. In *Physical Chemistry*; W.H. Freeman and Company: New York, 2006; pp 1005−1006.
(26) Wang, H.-H.; Zhou, Z.-Y.; Yuan, Q.; Tian, N.; Sun, S.-G. Pt Nanoparticle Netlike-Assembly as Highly Durable and Highly Active Electrocatalyst for Oxygen Reduction Reaction. *Chem. Commun.* **2011**, *47*, 3407−3409.
(27) Zhang, P. X-ray Spectroscopy of Gold-Thiolate Nanoclusters. *J. Phys. Chem. C* **2014**, *118*, 25291−25299.
(28) Lingane, J. J. Thermodynamic Significance of Polarographic Half-Wave Potentials of Simple Metal Ions at the Dropping Mercury Electrode. *J. Am. Chem. Soc.* **1939**, *61*, 2099−2103.
(29) Bonakdarpour, A. *A Combinatorial Study of Pt-Based Oxygen Reduction Electrocatalysts for Hydrogen Fuel Cells*; Dalhousie University: Halifax, NS, Canada, 2007.
(30) Song, C.; Zhang, J. Electrocatalytic Oxygen Reduction Reaction. In *PEM Fuel Cell Electrocatalysts and Catalyst Layers*; Springer: London, 2008; pp 91, 113.